Magnetic Resonance Imaging 63 (2019) 147–154

Contents lists available at ScienceDirect

Magnetic Resonance Imaging

journal homepage: www.elsevier.com/locate/mri

Original contribution

Parallel magnetic resonance image reconstruction from a single-element parametric amplifier

Roshan Timilsina, Chunqi Qian*

Department of Physics, Oakland University, Rochester, MI 48309, USA
Department of Radiology, Michigan State University, East Lansing, MI 48824, USA

ARTICLE INFO

Keywords:
Correlation
GRAPPA
Image reconstruction
Parallel MRI
Parametric amplifier
Signal-to-noise ratio
SoS
WAND

ABSTRACT

In magnetic resonance imaging (MRI), acquisition speed is always an important issue. In this paper, we propose a promising technique to achieve parallel MRI (pMRI) on a single-channel spectrometer, using a novel Wireless Amplified Nuclear MR Detector (WAND) for spatial encoding in image reconstruction. For this, a planar structure double frequency WAND is designed and fabricated, where two of its frequencies - '*signal*', ω_1 and '*idler*', ω_2 are effectively utilized as two separate "channels" for accelerated acquisition. We provided a thorough background needed for the method and subsequently parallel imaging algorithms. Sum-of-Squares (SoS) reconstruction and GeneRalized Autocalibrating Partially Parallel Acquisition (GRAPPA) reconstruction are used to reconstruct as well as to analyze the SNR in the resulting images and validate our hypothesis. Experimental results using phantom datasets demonstrate that the proposed method of parallel imaging yield a better sensitivity for the combined images ('*idler*' + '*signal*') than the sensitivity acquired for each individual image and thus significantly improving the reconstruction quality with optimal signal-to-noise ratio. We also demonstrated the achievable acceleration factor of this approach.

1. Introduction

Magnetic Resonance Imaging (MRI) is a commonly used non-invasive medical diagnostic tool. It utilizes a uniform magnetic field to polarize the sample, and a three-directional magnetic field gradient to encode spatial information into the uniquely-identifiable resonance frequency from different regions of sample, thus producing detailed images of organs, soft tissues, bone and almost all other internal body structures. However, the relatively long acquisition time needed to capture all the data may introduce image artifacts due to involuntary patient motion. The development of parallel MR imaging (pMRI) techniques [1–13] to accelerate MRI data acquisition has changed the way MRI is used in the clinic. This approach, however, requires extensive upgrades of spectrometer consoles from single-channel to multiple-channel acquisition [14–17]. In this research, we introduce a convenient method to achieve parallel acquisition on a single-channel spectrometer. By introducing a Wireless Amplified Nuclear MR (NMR) Detector (WAND) [18–26] that inductively couples with a single-element detection coil readily available on any scanner, we can utilize the signal mixing [27,28] capability of the WAND to differentiate signals detected by the WAND from those that are directly detected by the single-element coil, thus effectively multiplexing the channels for accelerated acquisition.

A WAND is a localized detector that can sensitively detect and simultaneously amplify MR signals, which are then wirelessly transmitted to a single-element detection coil with a direct wired connection to the spectrometer console. The WAND has an integrated parametric amplifier (paramp) [28–34] which can utilize nonlinear capacitance to transfer energy from the high energy pumping signal at ω_3 to the low energy MR signal at the Larmor frequency ω_1. When these two signals interact, the WAND can amplify the MR signal at the Larmor frequency and simultaneously convert it to another signal at the idler frequency, $\omega_2 = \omega_3 - \omega_1$. Our motivation is to assume and utilize the signals at both ω_1 and ω_2 as two separate channels for acceleration in pMRI reconstruction and demonstrate that combining these images yields a better sensitivity than the sensitivity acquired for each individual image.

Two methods of image reconstruction techniques are discussed to compare the sensitivity of these phase-shifted images assumed as phased array coils viz. sum-of-squares (SoS) reconstruction, and generalized autocalibrating partially parallel acquisitions (GRAPPA) reconstruction. Distinct images at the Larmor (ω_1) and the idler (ω_2) frequencies are combined using each of the image reconstruction techniques to optimize the signal-to-noise ratio (SNR). The different

* Corresponding author.
E-mail address: qianchu1@msu.edu (C. Qian).

https://doi.org/10.1016/j.mri.2019.08.009
Received 23 April 2019; Received in revised form 22 July 2019; Accepted 15 August 2019

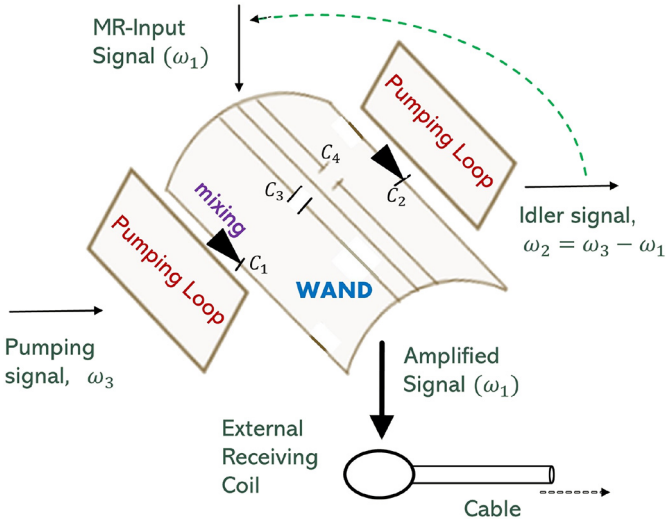

Fig. 1. Schematics of a square shaped (10 mm × 10 mm) double frequency WAND. C_3 and C_4 are the chip capacitors each of 12 pF value and C_1 and C_2 are the varactor diodes each of 22 pF value. A pair of horizontal rectangular loops driven by the same coaxial cable is used to feed pumping power to wirelessly activate the WAND. The WANDs higher frequency resonance mode is sensitive to this pumping power at ω_3. Its lower frequency resonance mode is sensitive to MR signals at ω_1 and the '*idler*' signal $\omega_2 = \omega_3 - \omega_1$ is created during parametric frequency mixing.

spatial information contained in the WAND and the coupled single-element coil can partially replace spatial encoding that would normally be performed using gradients, thereby reducing acquisition time.

2. Materials and methods

2.1. Principle of a WAND

The WAND has a built-in parametric amplifier [28–34], which operates on the principle of a parametric amplification. During RF transmission, the varactors C_1 and C_2 are modulated to detune the WAND by the strong excitation pulse. During signal reception, the varactors enables the weak MR signals at the Larmor frequency (ω_1) to mix with the strong pumping signal (ω_3) that is applied perpendicularly to create an amplified output at the idler frequency, $\omega_2 = \omega_3 - \omega_1$. This amplified output further mixes back with the pumping signal to create a second amplified output at ω_1, which can be detected by an external receiving coil (Fig. 1). This process is called parametric frequency mixing [27,28] and is crucial in parametric amplification. The WAND coil used in this study is a double frequency resonator [20,21,26] that can receive the MR signal at the Larmor frequency ω_1 and the pumping signal at approximately twice the Larmor frequency i.e., $\omega_3 \sim 2\omega_1$. The signal frequency ω_1 is used to acquire one image and is called the "*signal image*" and the idler frequency ω_2 is used to acquire another image called the "*idler image*". By setting the pumping frequency slightly above twice the signal frequency, we have two non-interfering signals – amplified MR signal at ω_1 and the generated idler signal at ω_2 – both being well below the pumping frequency ω_3. To detect simultaneously the MR signal and the idler signal, the imaging bandwidth should be kept large enough i.e. $BW > |\omega_3 - 2\omega_1|$.

2.2. Design of a WAND

The double frequency WAND circuit pattern is etched on a copper-clad polyimide foil. It has a total dimension of 10 × 10 mm^2 and a strip width of 0.5 mm. It consists of a continuous vertical leg in the center,

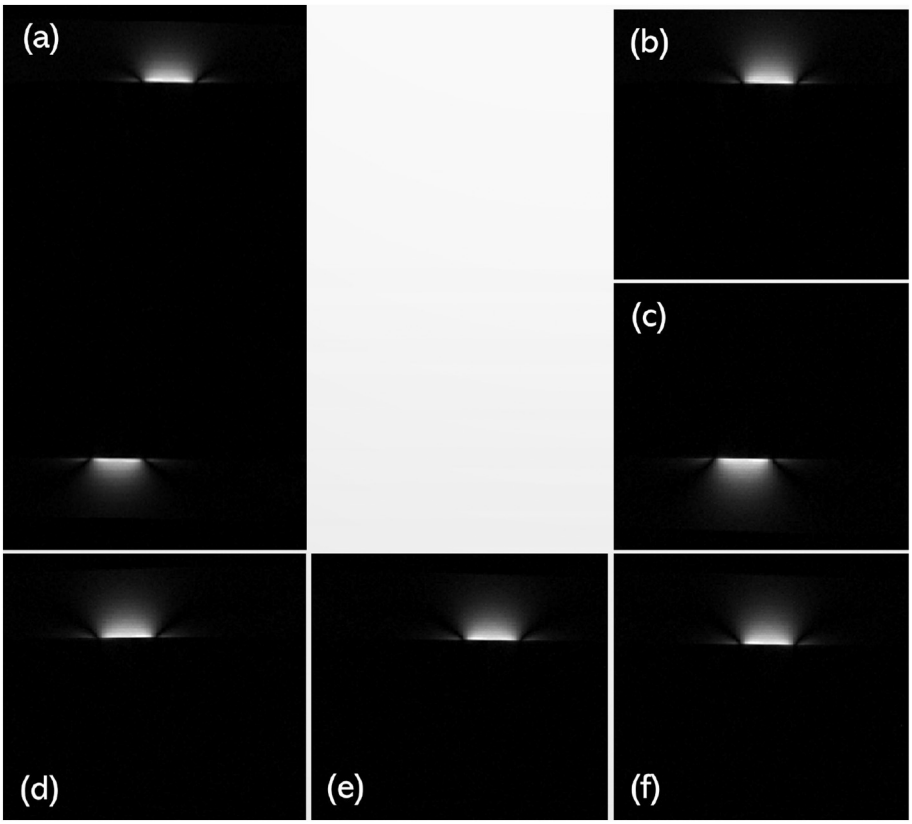

Fig. 2. Division and alignment of two '*idler*' and '*signal*' images. (a) Fully acquired initial image of size 512 × 256. (b), (c) 512 × 256 image matrix in (a) is divided into two equal parts each of size 256 × 256. (d), (e), (f) flipping and alignment of image matrix (c) with (b).

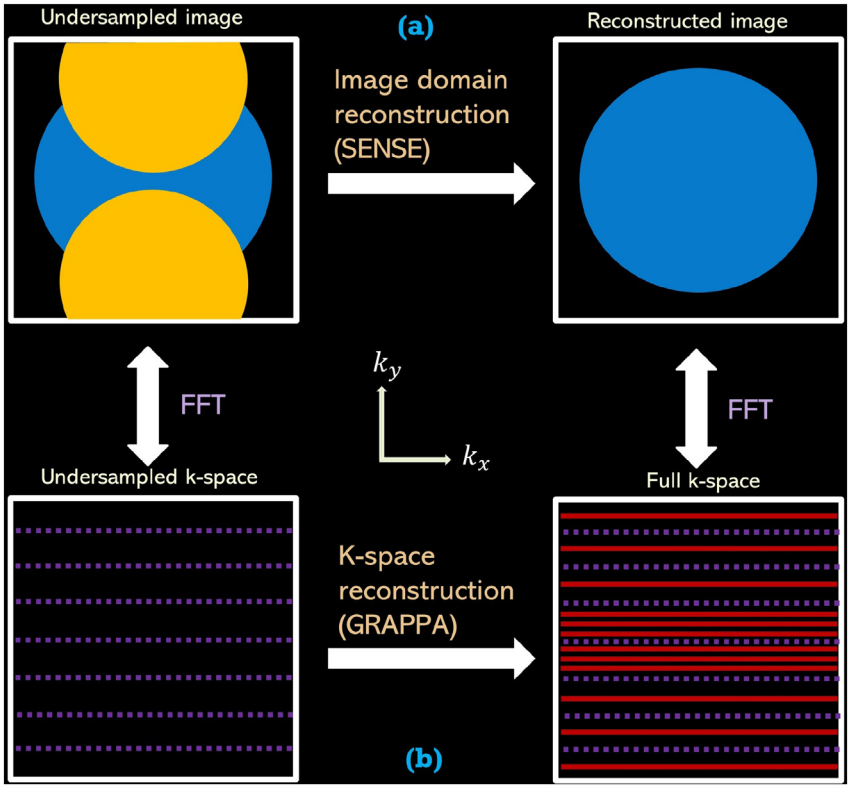

Fig. 3. A general description of parallel MRI. (a) In image domain reconstruction, firstly an aliased image is produced from the under-sampled *k*-space and then the full field-of-view image is produced by using the sensitivity maps of the coils. (b) In *k*-space reconstruction, the missing lines of *k*-space are estimated first and then inverse Fast Fourier Transform of this full *k*-space produces the reconstructed image.

and two split legs on its left and right, which are separated by 0.5 mm apart. These split legs are bridged by chip capacitors C_3 and C_4 with 12 pF capacitance. The varactor diodes C_1 and C_2 are 22 pF and are zero-biased [35]. The dipole resonance mode has a resonance frequency close to the Larmor frequency (ω_1) for a 7 T scanner, when the majority of the current flows around the circumferential conductor legs. In the low frequency butterfly resonance mode that is not used in our experiment, the majority of the current flows in the center continuous legs. In the high frequency butterfly resonance mode that is sensitive to the pumping signal, the out-of-phase currents flows through the two capacitors (C_3 and C_4) in the center.

2.3. Data acquisition for reconstruction

To test the WAND's performance, images of a water phantom were acquired on a 7 T MR system (Bruker Biospin Billerica, MA, USA) using the WAND coupled with a volume coil. A spoiled gradient refocused echo (SPGR) sequence was acquired, using TE = 4.4 ms, TR = 115.2 ms, flip angle = 35°, FOV = 16 cm × 8 cm, matrix size = 512 × 256, slice thickness = 0.8 mm, so that the entire FOV contains images at both ω_1 and ω_2. To fully utilize these two pieces of information, one of the images is flipped and shifted to align with the other. For this, we break the initial 512 × 256 matrix (Fig. 2a) into the top and bottom halves, each containing 256 × 256 matrix elements (Fig. 2b–c). The bottom image (Fig. 2c) is sequentially mirrored along the horizontal axis and the vertical axis to obtain Fig. 2d and e, respectively. Finally, the image in Fig. 2e is transposed horizontally to align perfectly with Fig. 2b. Images in Fig. 2b and f are the '*signal*' image and the transformed '*idler*' image used for subsequent processing. To be in accordance with conventional nomenclature, these two images are referred to as **'channel 1'** and **'channel 2'** for pMRI.

3. Implementation of parallel imaging algorithms

3.1. Sum-of-squares reconstruction theory

During image reconstruction process, sometimes it is desirable to have a technique that combines the data without detailed knowledge of the coil's magnetic fields or without computing the coil sensitivities and at the same time preserves the high SNR of the phased array [36]. The sum-of-squares (SoS) method has the advantage that it does not use the coils' positions or RF field maps, thus does not require prior knowledge of the sensitivities of the receiver coils. In this algorithm, the signal in each pixel in the composite image is the square root of the sum of the squares of the pixel values from the images from individual coils or channels. This would allow arriving at a method of combining images without computation or measurement of the magnetic fields.

More specifically, the pixel intensity in the reconstructed image is the square root of the sum of the squares of all the signal intensities at that position, as detected from each of the receiving elements. Thus, for n-channel detection, the measured pixel intensity in the composite image is given by [37–39]:

$$M_n = \sqrt{\sum_{k=1}^{n} (M_{rk}^2 + M_{ik}^2)} \quad (1)$$

where M_{rk} and M_{ik} represent the measured pixel intensities (sum of the signal and noise intensities) in the real and imaginary parts of the complex image reconstructed from the *k*th channel, respectively. To the degree that at least one coil in the array has a high pixel SNR and all coils have similar noise, combining the images as sum-of-squares results in a high SNR. The SoS reconstruction method, however lacks the phase information in the combined image.

3.2. GRAPPA reconstruction theory

Typically, there are two approaches of parallel MRI reconstruction methods. One is 'image' based and the other is the '*k*-space' based. Thus,

their stage of operation is different in the MR image reconstruction process in pMRI. A method that reconstructs images from each coil element with reduced FOV (more widely spaced lines) and then merges the images using knowledge of individual coil sensitivities is called sensitivity encoding (SENSE) and operates in the image domain (Fig. 3a). A method that explicitly calculates missing spatial frequency space (*k*-space) lines before Fourier transformation of the raw data during the MR reconstruction process is called GRAPPA and operates in the *k*-space (frequency) domain. In the GRAPPA reconstruction technique (Fig. 3b), a reduced number of *k*-space lines are acquired for each channel. For an acceleration factor of two, only every second line is acquired, and some additional *k*-space lines are also acquired at the center of the *k*-space for each channel. Then this fully sampled data at the center of the *k*-space is used to estimate the weights for the missing *k*-space lines. The weights calibrated in the previous steps are applied to estimate the missing *k*-space lines for each channel data. Finally, the inverse Fourier Transform of this full *k*-space data produces the final reconstructed image.

In contrast to SENSE, the GRAPPA reconstruction method uses an auto-calibration technique to determine the spatial sensitivities of individual channel coils in the phased array. The idea behind GRAPPA is to use portions of the acquired k-space to calculate the portions that are not acquired. The additional k-space lines in low frequency region, called the autocalibration signal (ACS) lines, are used to fit the coefficients of linear combinations. Next, the fitting coefficients are applied to estimate the missing k-space data by interpolation of acquired data. Finally, the image is recovered by using sum-of-squares (SoS) to combine all coil images [6]. A few extra phase encoding lines were introduced for autocalibration, so acceleration factors will be slightly lower and SNR decrease is also in proportion.

For a two-channel system, as shown in Fig. 4a, we seek to recreate the missing *k*-space lines using a combination of its neighbors, here two adjacent neighboring lines. To recreate those missing lines, we use the auto-calibration signal lines (dotted lines). The linear combination of the other two nearest lines from all channels would give the closest approximation to the auto calibrated signal (ACS) line from channel 1. Similarly, we need to evaluate what linear combination would yield the best approximation to the ACS line of channel 2. We then have the set of linear equations [40,41]:

$$S_{12} = C_{11}S_{11} + C_{13}S_{13} + C_{21}S_{21} + C_{23}S_{23} \quad (2)$$

$$S_{22} = D_{11}S_{11} + D_{13}S_{13} + D_{21}S_{21} + D_{23}S_{23} \quad (3)$$

where S_{12} and S_{22} are the *k*-space line 2 of channel 1 and channel 2, respectively, which are missing (targets) and need to be determined. C_{11}, C_{13}, C_{21}, C_{23}, and D_{11}, D_{13}, D_{21}, and D_{23} are the reconstruction coefficients (weights) for channel 1 and channel 2, respectively. S_{11}, S_{13}, S_{21}, and S_{23} are the acquired *k*-space lines (sources) in channel 1 and channel 2.

Equivalently, Eqs. (2)–(3) can be generalized and can be written in matrix notation form:

$$s^{non-acquired} = W.\ S^{acquired} \leftrightarrow s^{target} = W.\ S^{source} \quad (4)$$

where W is called the 'weighting factor' for each of the channel combinations. These weights can be estimated by a repetitive use of small regions through the ACS line that are sampled at the Nyquist rate without acceleration. Each of these small regions consists of some source lines and some target lines. This process would yield all the missing lines anywhere in the *k*-space once the coefficients are determined. Thus, we now have a full *k*-space for each channel, which are then Fourier transformed and combined into a single image using a standard SoS method [2,4]. Since the GRAPPA reconstruction uses a sum-of-squares reconstruction, the SNR efficiency of GRAPPA approaches the SNR efficiency of a sum-of-squares reconstruction for low acceleration factors.

This process of utilizing more than one acquired lines to reconstruct each missing line in GRAPPA is also called a 'blockwise reconstruction' [6]. As shown in Fig. 4b, a block is a single acquired line plus the non-acquired lines adjacent to it. By using multiple blocks of data to fit each missing line, GRAPPA incorporates more information into each reconstructed line, resulting in a substantially improved fit. Since the final image combination in GRAPPA is performed using a magnitude reconstruction, any phase-related issues are essentially eliminated. Thus, it generates no phase information.

Chang et al. [42] have extended the conventional GRAPPA reconstruction into a more robust nonlinear (NL) approach using the '*kernel*' method [43–45] to reduce the noise-induced error in conventional GRAPPA where regularization would not work efficiently. This NL-GRAPPA approach also evaluates the nonlinear relationship between the bias in the estimated GRAPPA coefficients and the noise in the measured ACS data due to the error-in-variable problem [42] in the calibration step. The acquired under-sampled *k*-space data are then

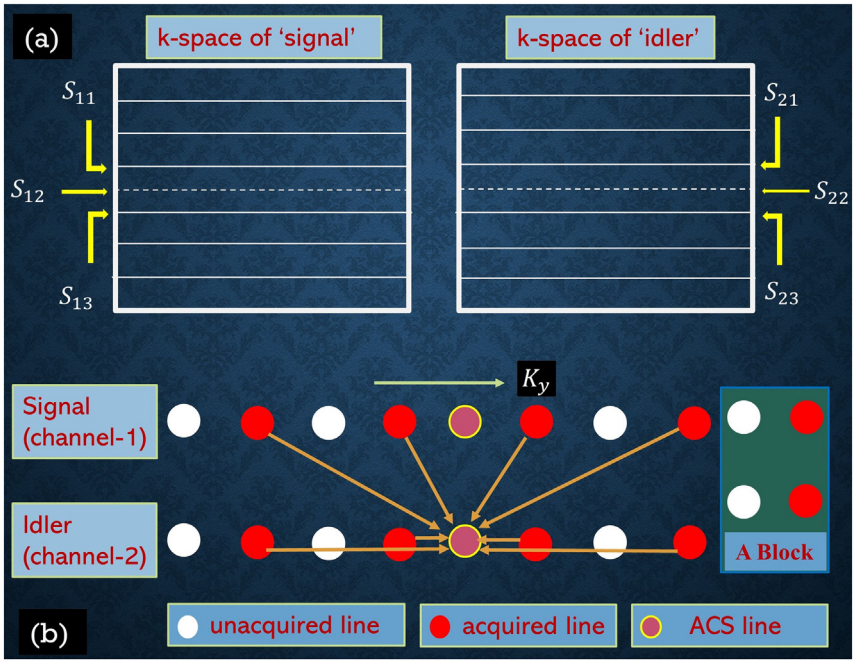

Fig. 4. Schematic description of GRAPPA parallel imaging method. (a) Undersampled *k*-space data for a two-channel system is shown by the solid lines. The dotted lines show the auto calibrated signal (ACS) lines. (b) GRAPPA uses multiple lines from all channels to fit one line in one channel (here channel 2). This procedure repeats for every channel, resulting in uncombined channel images, which can be finally combined using a sum of squares reconstruction. (Note: each dot represents a line in *k*-space).

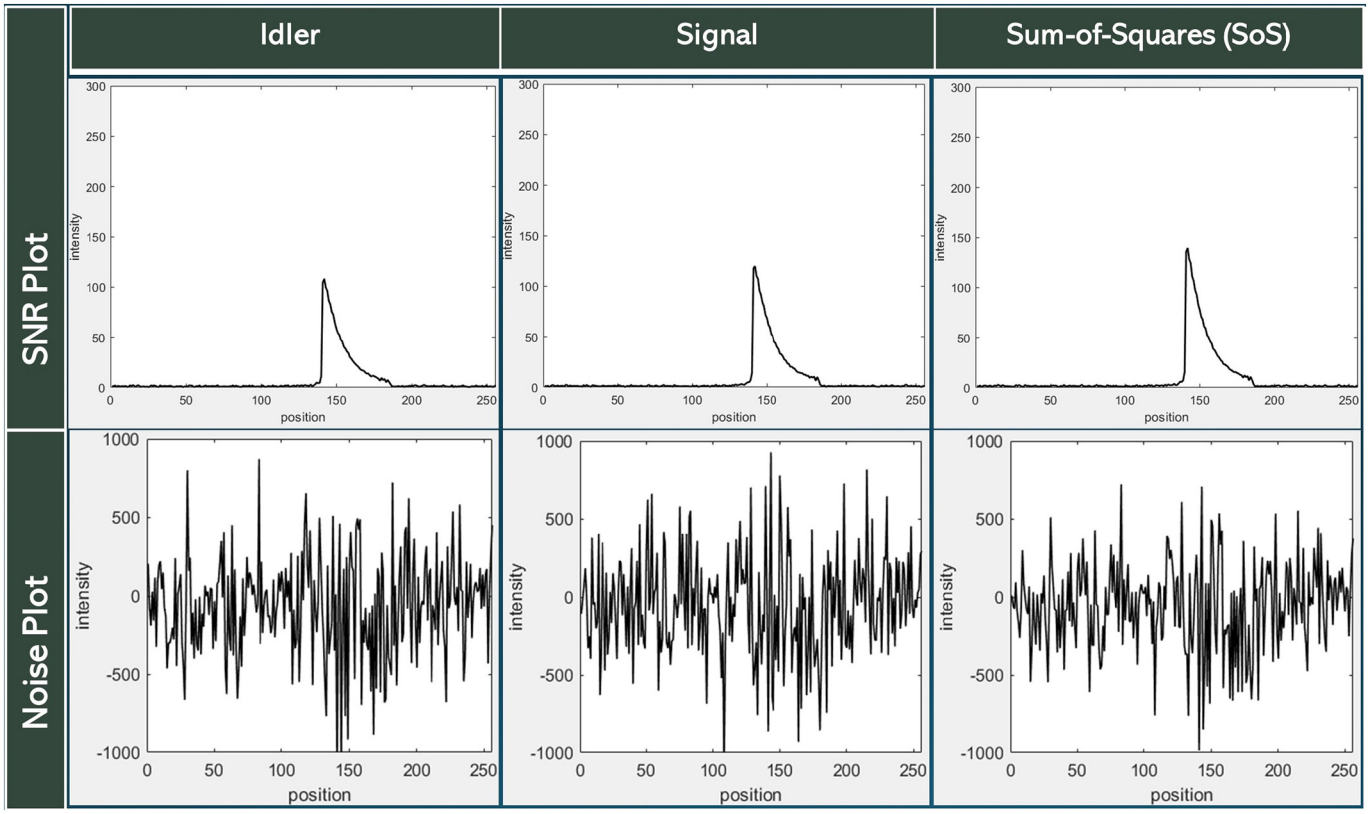

Fig. 5. 1D profiles of MR signal intensity through the image center and the corresponding noise plots for uncombined coil images and resultant images obtained by SoS reconstruction.

mapped through a nonlinear transformation to a high-dimensional feature space and then linearly combined to estimate the missing *k*-space data.

To understand the effect of noise in regression and prediction of GRAPPA in Eq. (4), nonlinear GRAPPA introduces latent variables [46].

$$\begin{aligned} S &= \widetilde{S} + \delta_S \\ s &= \widetilde{s} + \delta_s \\ f &= \widetilde{s} = \widetilde{S}\widetilde{W} \end{aligned} \tag{5}$$

where $\widetilde{S}$ and $\widetilde{s}$ represents the true, noise-free data points in the ACS and in the missing lines respectively. δ_S and δ_s are the measurement noises present in the ACS data and in the missing lines, which are assumed to be independent of the true value $\widetilde{S}$ and $\widetilde{s}$. $\widetilde{W}$ are the latent true coefficients without any hidden noise in the linear relationship. Coefficients W in Eq. (4) are estimated by fitting to the observed data in S and s:

$$s = S.\ W \rightarrow \widetilde{s} + \delta_s = (\widetilde{S} + \delta_S).\ W \tag{6}$$

Therefore, there is a bias $\delta_W = (W - \widetilde{W})$ in the coefficients estimated from the least-squares fitting. Since the bias depends on the noise in both S and s, its effects on the estimated coefficients W also depends on the noise. Thus, the bias in the ACS is not a linear function of the noise, which leads to the errors-in-variable problem in regression analysis. These presented errors in the reconstruction process are given by [42,47]:

$$y - \widetilde{S}\widetilde{W} = (\widetilde{S} + \delta_S).\ (\widetilde{W} + \delta_W) \tag{7}$$

which implies the biased coefficients for the estimated missing *k*-space data is nonlinear and with noise. These nonlinear errors are then solved using '*kernel*' approach used in machine learning, which allows algorithms to be nonlinear through simple modifications in linear problem. With a nonlinear mapping, Eq. (4) is then transformed to a new linear regression equation as follows:

$$s^{non-acquired} = \phi(S^{acquired}).\ W \tag{8}$$

where kernel is given by [42]:

$$k(S_1, S_2) = < \phi(S_1, S_2) > S_1,\ S_2 \in S \tag{9}$$

as the inner product between S_1 *and* S_2 and

$$\phi(\mathrm{S}) = [\phi(S_1), \phi(S_2), \ldots\ldots, \phi(S_k)]^T \tag{10}$$

S_1, S_2, . . …, S_k are the row vectors of matrix S in Eq. (4). Eq. (8) describes the nonlinear relationship between the undersampled *k*-space data in S and missing data in s.

As usual, coefficients W can be solved using a least-squares method in a feature space [42]:

$$W = (\phi^{\mathrm{T}}(\mathrm{S})\phi(\mathrm{S}))^{-1}\phi^{\mathrm{T}}(\mathrm{S}).\ s \tag{11}$$

These W's are then substituted in Eq. (8) to reconstruct the missing data in the outer *k*-space.

In cases where it is difficult to make a reliable sensitivity map (such as in heterogeneous regions) or when differences exist between acquisition for sensitivity mapping and the imaging sequence (such as echo-planar imaging that is more sensitive to magnetic susceptibility artifacts), algorithms of the GRAPPA type are preferred over SENSE.

4. Image analysis: SNR measurement in reconstructed MR images

The signal-to-noise-ratio (SNR) is an important quantity used to describe the performance of a magnetic resonance imaging (MRI) system and is frequently used for image evaluation. From two identical image acquisitions k_1 and k_2, the average SNR in a region-of-interest (ROI) can be determined as [48–51]:

$$SNR_{diff}(k_1,k_2) = \frac{S_{diff}}{\sigma_{diff}} = \frac{\frac{1}{2}mean[S_N(r,k_1) + S_N(r,k_2)]}{\frac{1}{\sqrt{2}}stdev[S_N(r,k_1) - S_N(r,k_2)]} = \frac{1}{\sqrt{2}}\frac{m_{sum}}{S_{diff}} \quad (12)$$

where m_{sum} is used as an abbreviation for a sum of mean values for two acquisitions and S_{diff} is the standard deviation of the intensity difference between the two acquisitions. Thus, the SNR_{diff} in an ROI is calculated as the quotient of the mean value of the signal at certain ROI in the sum image and the standard deviation evaluated in the same ROI in the difference image, divided by $\sqrt{2}$.

The SNR performance of each reconstructed images (SoS, and GRAPPA) at different acceleration factors for a WAND coil are then evaluated.

5. Results

5.1. Sum-of-squares reconstruction

As is clear from Fig. 5 that in each of the reconstructed method, "idler" image has the lowest SNR and highest noise, because it only contains signal contribution from the WAND. The signal image has higher SNR than the idler image because it also contains signal contribution from the external receiving coil. The SoS-combined image has the highest SNR performance and correspondingly the lowest noise.

5.2. Nonlinear GRAPPA reconstruction

Computer simulation was performed to establish the SNR performance of nonlinear GRAPPA at different acceleration factors for a combined idler and signal imaging array. Fig. 6 shows the reconstructions of the phantom images using sum-of-squares as reference image and a nonlinear GRAPPA for a reduction factor (R) = 2, 4, 8, number of coils = 2, and the ACS lines of 42. The first column shows the SoS and GRAPPA images for various accelerations. The second column shows the reconstructed image acquired at identical conditions. The convolution size of the coefficients for the algorithm used was 2 blocks and 15 columns. It is seen that the GRAPPA reconstruction image acquired using $R = 8$ ($R_{net} = 3.71$) has largest noise, whereas reduced value of acceleration ($R = 4$, $R_{net} = 2.71$ and $R = 2$, $R_{net} = 1.71$) has better SNR. For low reduction factor (in our case 2), GRAPPA reconstruction method suppresses most of the noise without additional artifacts or loss of resolution. The SNR on a pixel-by-pixel basis is then calculated from Eq. (12).

Fig. 7 shows the intensity plot and the corresponding noise plots for each of the three cases with acceleration factors 2, 4, 8 and for a reference image obtained by Sum-of-Square. Unambiguously, we could see that at high acceleration factor (R = 8) GRAPPA reconstruction suffers from a high level of noise and thus low SNR peak (66 units) even with a large number of auto-calibration signal lines. In contrast, for a low value of acceleration, significant improvement in SNR and noise is evident (R = 4 SNR peak is 111-units, $R = 2$ peak is 145 units). Fig. 8 shows the relationship between acceleration factor and SNR using the nonlinear GRAPPA algorithm for various acceleration factors ranging from 2 to 8. It is clear that the SNR deteriorates abruptly as the acceleration factor is increased. It should also be noted that in the limit where all the *k*-space lines are acquired, GRAPPA approaches the sum-of-squares reconstruction, so that nearly no loss in performance is expected, especially for low acceleration factors. This is evident from our result comparing the SNR for $R = 2$ in GRAPPA and the SNR for the reference image whose performance are almost identical.

6. Discussion

Previously, WANDs were developed as implantable or interventional detectors [19,21,22] to more sensitively observe deep lying tissues. As WANDs are essentially devices to accurately observe and diagnose deep lying body structures, the use of them in pMRI would have substantial implications, as parallel imaging alone still has its own limitations to obtain sufficient signal sensitivities in target regions deep inside the body. In this article, we studied the application of parametric amplification [33,34] in parallel MR imaging. For this, we have built a planar structure double frequency WAND and utilized the novel concept that both the "*signal*" and the "*idler*" could be subsequently used as two signal channels for accelerated acquisition. We have successfully implemented the two "**channels**" in a sum-of-squares combination, and nonlinear GRAPPA for sensitivity study and demonstrated that combining two images enables acceleration in GRAPPA. Further, we have found that GRAPPA images contain larger artifacts when the acceleration factor is increased beyond 4. In addition, we have shown that GRAPPA approaches the sum-of-squares reconstruction in the limit where all the *k*-space lines were acquired.

To discuss the extent that the noise spectra in the two WAND channels are correlated, in parametric frequency mixing approach it should be noted that the two channels - 'signal, ω_1' and 'idler, ω_2' are not truly independent as both the signals are derived from the same MR input signal at ω_1, which is the operating frequency of MR scanner. Fig. 9 shows the noise covariance matrix (NCM) for the two-channel

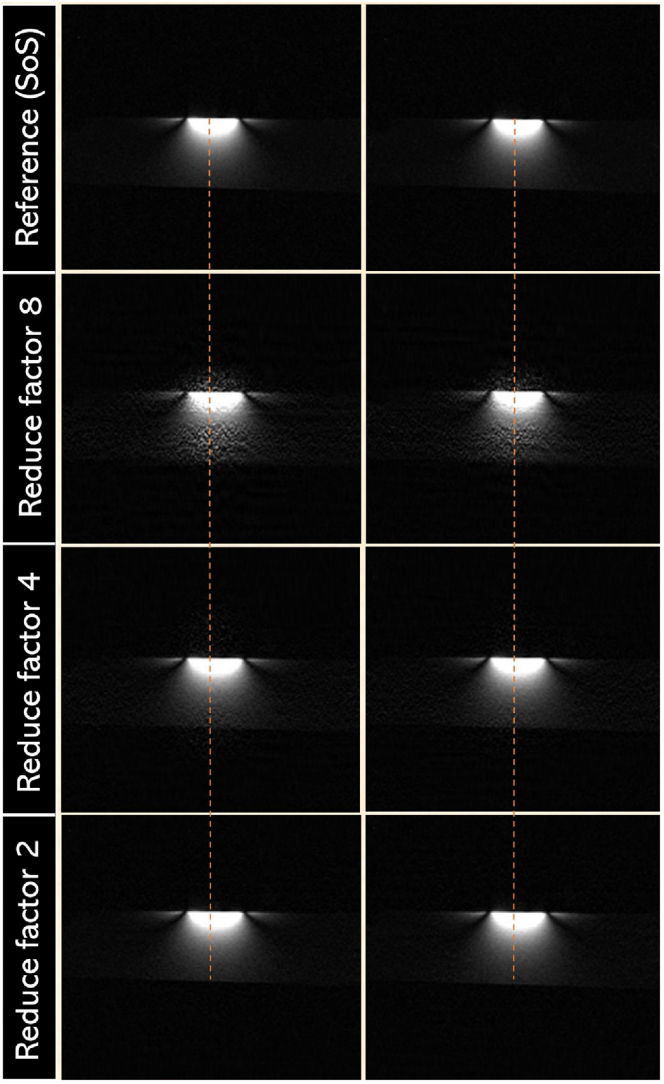

Fig. 6. Phantom images acquired from two-channel datasets reconstructed using nonlinear GRAPPA with a reduction factor of 2, 4, 8 and 42 ACS lines. The vertical dashed lines through the images indicate position.

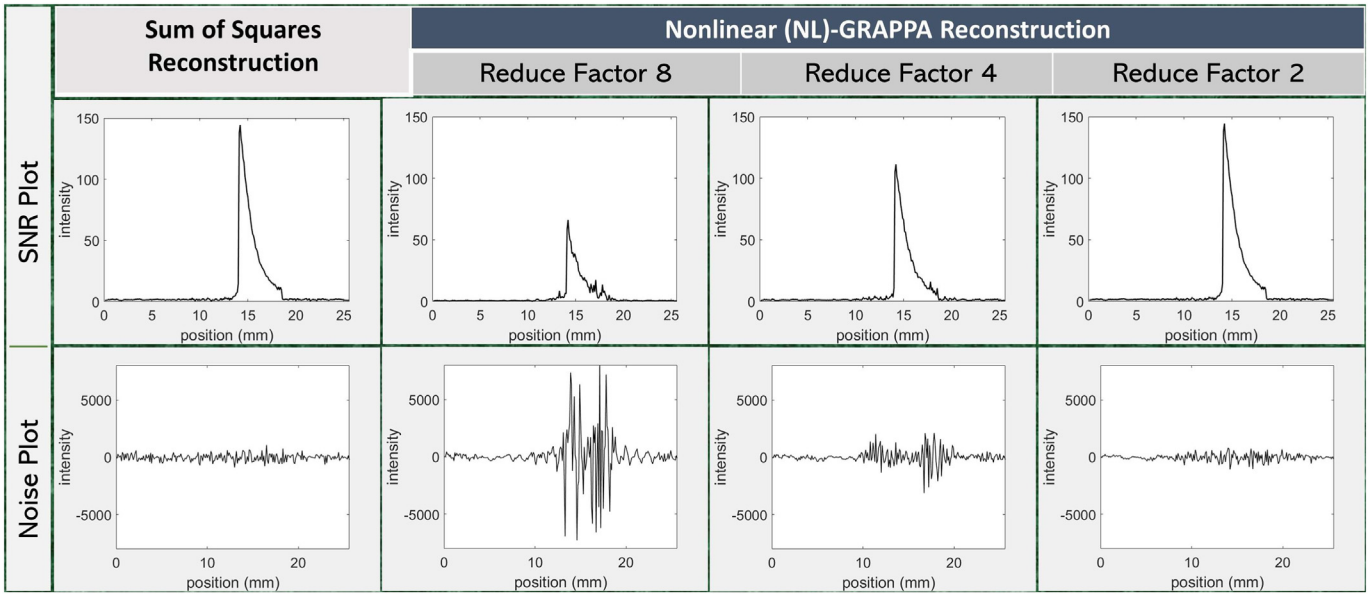

Fig. 7. SNR profile and the intensity difference plots obtained for a combined coil images for SoS reconstruction, and nonlinear GRAPPA reconstruction for three various reduction factor values (R = 2,4, and 8).

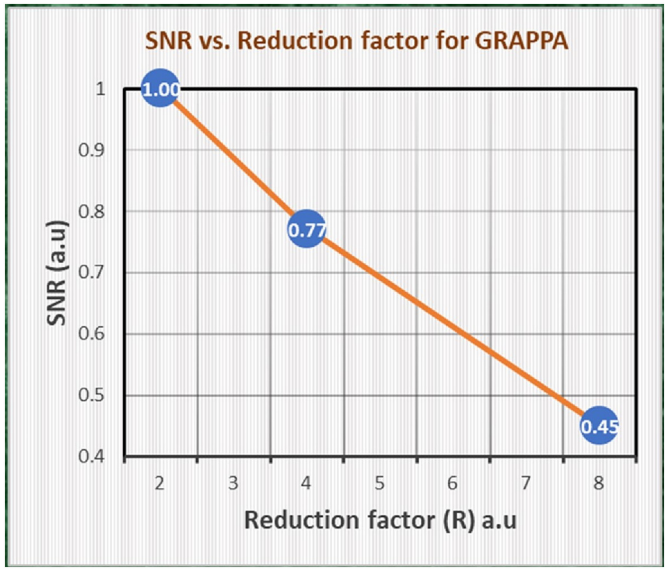

Fig. 8. NL-GRAPPA SNR peak heights from Fig. 7 are taken and plotted as a function of the reduction factor (R).

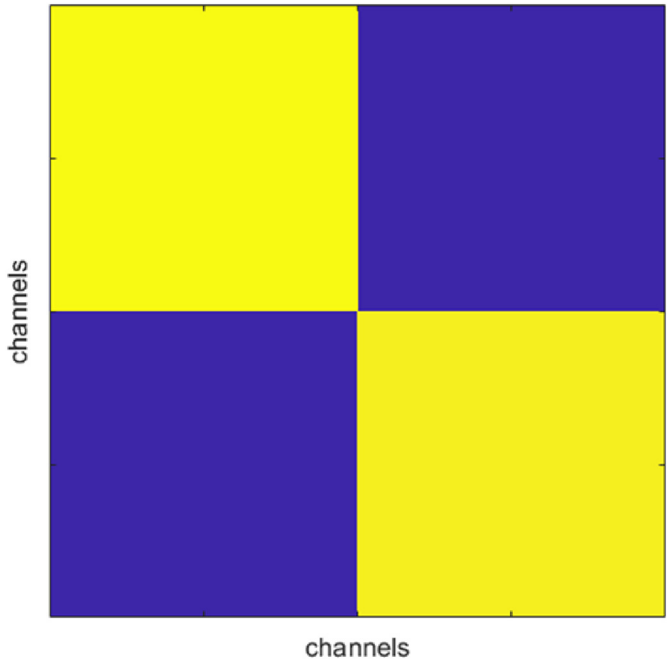

Fig. 9. Graphical rendering of the 2 × 2 size noise covariance matrix (NCM) of the 2-channel parallel imaging system array.

coil system. By subtracting two identical images, we calculated the noise covariance matrix between the noise at both the signal and idler frequencies. The graphical representation of the noise covariance matrix obtained in Fig. 9 can be written in a matrix form:

$$\Sigma = \begin{bmatrix} \sigma(x,x) & \sigma(x,y) \\ \sigma(y,x) & \sigma(y,y) \end{bmatrix} = 1000_{*} \begin{bmatrix} 5.8429 & 1.9664 \\ 1.9664 & 5.7113 \end{bmatrix} \quad (13)$$

The diagonal elements in Σ in expression (13) depicts the variance of the variable. The off-diagonal elements depict the covariance between all possible pairs of variables, and they characterize how the noise correlation is between the two channels. It is seen that the noise covariance matrix of the 2-element array shows slight differences in the noise levels between the two channels and some correlations between the elements as characterized by non-zero off-diagonal elements. The quality of the reconstructed image is compromised if the noise between coil elements is correlated [52]. In our case, the noise correlation between the coil elements showed correlations of around 34% so certainly there should be some compromise in the quality of the reconstructed image, but not significantly. These two "channels" contain different information because the "idler" image only contains contribution from the WAND while the "signal" image, in addition, contains contribution from the external volume coil. Given, if the two coil elements are completely correlated, the SNR of two channels should be the same as the SNR of a single channel. On the other hand, if these are completely uncorrelated then the SNR of two channels should be 1.414-fold larger than the SNR of a single channel. Since there is some partial correlation of 34% between the coils, SNR of two channels should be $\frac{1.414}{\sqrt{1+0.34}} = 1.22$ times the SNR of a single channel. Upon measuring the SNR plots peak height in the "Signal" and "Sum-of-Squares" obtained in

Fig. 5, the combined SoS reconstructed image still has $\frac{139.3}{119.9} = 1.16$ fold larger SNR than the single channel which is in reasonable agreement with our prediction [53].

Ideally, signal-to-noise in FT-NMR is determined by the noise figure of the first pre-amplifier. However, because the WAND is made small enough to improve local sensitivity, it is in the coil-noise dominant region. For robust operation, its gain level is normally tuned to ~15 dB, which is sometimes not sufficient to completely suppress the noise on the external volume coil. Under this circumstance, the addition of "idler" image could improve sensitivity over "signal" image alone. In addition, because the pumping frequency is far separated from the Larmor frequency, by incorporating a bandpass filter in front of the pumping signal, slight fluctuation in the pumping power could be well separated and removed from the image spectral window.

We have reconstructed the original image without prior knowledge of the sensitivity functions in the sum-of-squares (SoS). The SoS method assumes that the sum of the absolute squares of all sensitivity functions are spatially uniform such that the spatially varying sensitivity weighting is removed [39]. Because the SoS-combined image has higher SNR than the "*signal*" image, these two channels certainly contain non-redundant information. In addition to sensitivity improvement, we have also utilized their non-redundancy for accelerated acquisition. The nonlinear GRAPPA employs an auto-calibration technique for receiving coil sensitivities [42], which requires no explicit computation of sensitivity maps as in SENSE.

7. Conclusion

We have demonstrated that the two frequencies – "*idler*" and "*signal*" from the parametric mixing process could be used to generate two separate "**channels**" for pMRI. These two channels when combined together yields better sensitivity than uncombined images though the noise spectra in the two WAND channels are correlated to some extent. Further, these two separate channels provide the ability to accelerate in parallel imaging. This convenient strategy of parallel imaging that requires no extensive upgrade of spectrometer consoles may have potential clinical implications such as in brain imaging, dynamic cardiac imaging and functional MRI (fMRI).

Funding

This work was supported by the National Institutes of Health [grant number R00EB016753].

References

[1] Wang H. Accelerating MRI data acquisition using parallel imaging and compressed sensing. Theses and Dissertations 2012:207].
[2] Omer H. Parallel MRI: tools and application. Imperial College London; 2012. Doctoral Dissertation.
[3] Aja-Fernández S, Vegas-Sánchez-Ferrero G, Tristán-Vega A. Noise estimation in parallel MRI: GRAPPA and SENSE. Magn Reson Img Apr 2014;32(3):281–90.
[4] Deshmane A, et al. Parallel MR imaging. J Magn Reson Imaging 2012;36(1):55–72.
[5] Chang Y, et al. Nonlinear GRAPPA: a kernel approach to parallel MRI reconstruction. Magn Reson Med 2012;68(3):730–40.
[6] Griswold MA, et al. Generalized autocalibrating partially parallel acquisitions (GRAPPA). Magn Reson Med 2002;47(6):1202–10.
[7] Blaimer M, et al. SMASH, SENSE, PILS, GRAPPA: how to choose the optimal method. Magn Reson Imag 2004;15(4):223–36.
[8] Ying L, Sheng J. Joint image reconstruction and sensitivity estimation in sense (JSENSE). Magn Reson Med 2007;57(6):1196–202.
[9] Glockner JF, et al. Parallel MR imaging: a user's guide. Radiographics 2005;25(5):279–97.
[10] Griswold MA, et al. Partially parallel imaging with localized sensitivities (PILS). Magn Reson Med 2000;44(4):602–9.
[11] Pruessmann KP, et al. SENSE: sensitivity encoding for fast MRI. Magn Reson Med 1999;42(5):952–62.
[12] Ying L, Liang ZP. Parallel MRI using phased array coils. IEEE Signal Proc Magaz 2010;27(4):90–8.
[13] Manning WJ, Sodickson DK. Simultaneous acquisition of spatial harmonics (SMASH): fast imaging with radio frequency coil arrays. Magn Reson Med 1997;38(4):591–603.
[14] Porter JR, Wright SM. A sixteen-channel multiplexing upgrade for single channel receivers. Magn Reson Imag 2001;19(7):1009–16.
[15] Porter JR, Wright SM, Famili N. A four-channel time domain multiplexer: a cost-effective alternative to multiple receivers. Magn Reson Med 1994;32(4):499–504.
[16] He W, et al. Four-channel magnetic resonance imaging receiver using frequency domain multiplexing. Rev Sci Instrum 2007;78(1):015102.
[17] Porter JR, Wright SM. Parallel acquisition of MR images using time multiplexed coil. IEEE Electr Lett 1992;28(1):71–2.
[18] Qian C, et al. Sensitivity enhancement of remotely coupled NMR detectors using wirelessly powered parametric amplification. Magn Reson Med 2012;68(3):989–96.
[19] Qian C, et al. Wireless amplified nuclear MR detectors (WAND) for high-spatial-resolution MR imaging of internal organs: preclinical demostration in a rodent model. Radiol 2013;268(1):228–36.
[20] Zeng X, et al. Wireless amplified NMR detector for improved visibility of image contrast in heterogeneous lesions. NMR Biomed 2018;31(9):1–9.
[21] Qian C, et al. Live nephron imaging by MRI. Americ J Physiol - Ren Physiol 2014;307(10):F1162–8.
[22] Zeng X, et al. Wireless MRI colonoscopy for sensitive imaging of vascular walls. Sci Rep 2017;4228:1–7.
[23] Zeng X, et al. Sensitive enhancement of vessel wall imaging with an endoesophageal wireless amplified NMR detector (WAND). Magn Reson Imag 2017;78(5):2048–54.
[24] Qian C, et al. Engineering novel detectors and sensors for MRI. J Magn Reson 2013;229:67–74.
[25] Timilsina R, Fan B, Qian C, et al. Signal sensitivity enhancement of high-spatial-resolution MR imaging with a concatenated cylindrical parametric RF-resonator. IEEE Sens J 2019. https://doi.org/10.1109/JSEN.2019.2894298.
[26] Timilsina R, Qian C. A novel expandable catheter wireless amplified NMR detector for MR sensitivity accessing the kidney in rodent model. IEEE Trans Biomed Circ Syst 2019;13(2):444–53.
[27] Bollenbeck J., Hergt M., Vester M., "Mixer circuit with balanced frequency mixer with varacter diodes". US Patent 7606551B2, 2009.
[28] Harwood L. A., and Tomomi M., "Parametric amplifier frequency up-converter". US Patent US3261981A, 1962.
[29] Collin RE. Foundation for microwave engineering. Wiley-IEEE Press; 2001.
[30] Syms RRA, et al. Parametric amplification of magnetic resonance images. IEEE Sens J 2012;12(6):1836–45.
[31] Qian C, et al. Integrated detection, amplification and wireless transmission of MRI signal using a parametric amplifier. Proc Int Soc Magn Reson Med. 2011.
[32] Hulbert AP. Upconverter. US Patent US8324901B2. 2012.
[33] Cork P. Hulbert A. P., Hunt J., "Parametric amplifier device". US Patent US8638102B2, 2014.
[34] Macpherson AC. Parametric amplifers and upconverters. NRL report 6024. 1964.
[35] Whelehan J., "Pump generated bias for parametric amplifiers". US Patent US3824482A, 1974.
[36] Roemer PB, et al. The NMR phased array. Magn Reson Med 1990;16(2):192–225.
[37] Constantinides CD, Atalar E, McVeigh ER, et al. Signal-to-noise measurements in magnitude images from NMR phased arrays. Magn Reson Med 1997;38(5):852–7.
[38] Larsson EG, et al. SNR-optimality of sum-of-squares reconstruction for phased-array magnetic resonance imaging. J Magn Reson 2003;163(1):121–3.
[39] She H, et al. Image reconstruction from phased-array MRI data based on multi-channel blind deconvolution. 2010 IEEE Int Symp biomed Imag: Nano macro. 2010. Rotterdam, Netherlands.
[40] Hashemi RH, Bradley WG, Lisanti CJ. MRI: The basics. Philadelphia, PA: Lippincott Williams & Wilkins; 2010.
[41] Griswold MA. Field-of-view limitations in parallel imaging. Magn Reson Med 2004;52(5):1118–26.
[42] Chang Y, Liang D, Ying L. Nonlinear GRAPPA: a kernel approach to parallel MRI reconstruction. Magn Reson Med 2012;68(3):730–40.
[43] Tomaso P, Steve S. The mathematics of learning: dealing with data. 2005 Intl Conf Neur Netw Brain, Beijing, China. 2005.
[44] Liu W, Pokharel PP, Principe JC. The kernel least-mean-square algorithm. IEEE Trans Signal Process 2008;56(2):543–54.
[45] Camps-Valls G, et al. Kernel methods in bioengineering, signal and image processing. London: Idea Group Publishing; 2007.
[46] Carreira-Perpin MA. Continuous latent variable models for dimensionality reduction and sequential data reconstruction PhD Thesis UK: University of Sheffield; 2001.
[47] Aja-Fernandez S, Tristan-Vega A, Scott Hoge W. Statistical noise analysis in GRAPPA using a parameterized noncentral Chi approximation model. Magn Reson Med 2011;65(4):1195–206.
[48] Dietrich O, et al. Measurement of signal-to-noise ratios in MR images: influences of multichannel coils, parallel imaging, and reconstruction filters. J Magn Reson Imag 2007;26(2):375–85.
[49] Wu B, et al. Comparison of SNR calculation methods for in vivo imaging. Proc Intl Soc Mag Reson Med. 2010. CA, USA.
[50] McCann AJ, Workman A, McGrath C. A quick and robust method for measurement of signal-to-noise ratio in MRI. Phys Med Biol 2013;58(11):3775–90.
[51] Reeder SB. Measurement of signal-to-noise ratio and parallel imaging. Parallel imaging in clinical MR applications. New York: Springer; 2007. p. 49–61.
[52] Hansen MS, Kellman P. Image reconstruction: an overview for clinicians. J Magn Reson Imag 2015;41(3):573–85.
[53] Larsson EG. SNR-optimality of sum-of-squares reconstruction for phased-array magnetic resonance imaging. J Magn Reson 2003;163(1):121–3.